ACS APPLIED MATERIALS & INTERFACES

www.acsami.org Research Article

Nanoporous Silicon Thin Film-Based Hydrogen Sensor Using Metal-Assisted Chemical Etching with Annealed Palladium Nanoparticles

Hyeonggyun Kim, Jeonghoon Yun, Min Gao, Hyeok Kim, Minkyu Cho, and Inkyu Park*

Cite This: ACS Appl. Mater. Interfaces 2020, 12, 43614−43623

Read Online

ACCESS | Metrics & More | Article Recommendations | Supporting Information

ABSTRACT: This article reports a nanoporous silicon (Si) thin-film-based high-performance and low-power hydrogen (H_2) sensor fabricated by metal-assisted chemical etching (MaCE). The nanoporous Si thin film treated with Pd-based MaCE showed improvement over a flat Si thin film sensor in H_2 response ($\Delta I/I_0$ = 4.36% → 12.4% for 0.1% H_2). Furthermore, it was verified that the combination of thermal annealing of Pd and subsequent MaCE on the Si thin film synergistically enhances the H_2 sensitivity of the sensor by 65 times as compared to the flat Si thin film sensor ($\Delta I/I_0$ = 4.36% → 285% for 0.1% H_2). This sensor also showed a very low operating power of 1.62 μW. After the thermal treatment, densely packed Pd nanoparticles agglomerate due to dewetting, which results in a higher surface-to-volume ratio by well-defined etched holes, leading to an increase in sensor response.

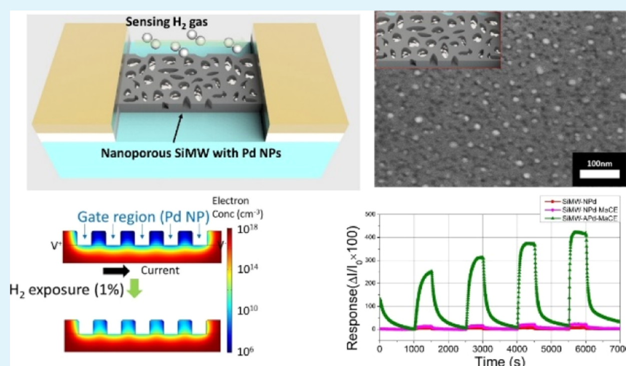

KEYWORDS: *hydrogen sensor, palladium nanoparticle, metal-assisted chemical etching, porous silicon, silicon microwire*

Downloaded via KOREA ADVANCED INST SCI AND TECHLGY on January 8, 2021 at 03:23:58 (UTC).
See https://pubs.acs.org/sharingguidelines for options on how to legitimately share published articles.

1. INTRODUCTION

Silicon (Si) has attracted interest from researchers in various applications such as optoelectronics,[1,2] energy conversion,[3] battery materials,[4] and chemical[5,6] and biological[7] sensors. Because of tunable electrical and optical properties of Si by doping, it is considered as one of the most promising materials for many nanoelectronic and sensing applications. In addition, the compatibility of Si with very-large-scale integration and complementary metal-oxide-semiconductor (CMOS) technologies is a considerable advantage over other materials.[8]

Si nanostructures such as Si nanowires (SiNWs),[9] Si nanopillars,[10] or porous Si[11] have high surface-to-volume ratios. This enhances the diffusion, adsorption, and desorption of the target molecules, which make them good candidates for sensing applications.[12] Among them, SiNWs have been greatly investigated for the last 2 decades because of their potential for high-performance chemical and biological sensors. Their detection mechanism is based on the change of charge density induced by the chemical gate effect.[13] The chemically modified surface of SiNWs acts as a chemical gate so that the chemical field-effect-transistor-type sensor responds to the target gas molecules. For example, palladium (Pd) is a typical chemical gate material for hydrogen (H_2) detection owing to its special absorption characteristics for H_2 gas, which can generate a change in the electric field on the SiNW surface.[14−17]

The fabrication methods of SiNWs can be classified into top-down[16] and bottom-up approaches.[18] Typically, bottom-up synthesis can produce high-quality nanostructures with a relatively lower cost.[19] However, this approach can achieve neither large-scale reproducibility nor easy device integration. A common and up-to-date way to fabricate top-down SiNWs is to use high-resolution lithography techniques such as electron beam lithography[17] and deep ultraviolet lithography.[16] Although it is possible to achieve nanostructures with good reproducibility by these high-resolution lithography methods, their high fabrication costs are unavoidable, which makes the low-cost mass production difficult.

Alternative cost-effective methods such as deep reactive ion etching,[20] block copolymer,[21] nanosphere lithography,[15] and metal-assisted chemical etching (MaCE)[22] have been suggested to fabricate top-down SiNWs. Among them, MaCE is a low-cost, top-down fabrication technique for vertical nanowire array or porous Si. MaCE is fast and facile since it is based on etching with noble metals and a mixture of hydrofluoric acid (HF) and oxidizing agents such as hydrogen peroxide (H_2O_2). MaCE has a few advantages such as (i) compatibility with CMOS techniques, (ii) good control over the shape of the Si nanostructure, and (iii) versatile selection of etchants.[23] Vertically aligned SiNWs by the MaCE method can

Received: June 13, 2020
Accepted: September 1, 2020
Published: September 1, 2020

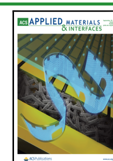

© 2020 American Chemical Society

https://dx.doi.org/10.1021/acsami.0c10785
ACS Appl. Mater. Interfaces 2020, 12, 43614−43623

be utilized as gas sensors with high response.[24] However, these gas sensors based on vertically aligned SiNWs rely on the random networks of nanowires. In addition, leakage current through the bottom Si substrate is unavoidable. Also, stable contact with electrodes is difficult due to structural weakness.

In this paper, we report an alternative usage of MaCE in the fabrication of nanoporous Si thin film, instead of vertically aligned SiNWs, to achieve high-performance, low-cost, and structurally robust H_2 sensors (Figure 1). In particular, Si thin film (thickness ~ 50 nm) decorated with palladium nanoparticles (Pd NPs) was employed to create Si nanostructures with etched holes. Typical MaCE methods result in Si nanostructures with microscale height with high etching speed (0.5−5 μm/min), which is too high for a Si thin film.[11] We adjusted the ratio of the oxidizing agent in an etchant to create holes with depths of a few tens of nanometers. In addition, Pd NPs were annealed by the rapid thermal annealing (RTA) process to induce solid-state dewetting of Pd NPs, which leads to aggregation of the NPs[25] and an increase of the distances between them. The purpose of annealing was to create a nanoporous surface after etching, rather than a surface with small roughness. MaCE with annealed Pd NPs provided a high response to H_2 gas, which is 60 times higher than that of a flat Si thin film sensor fabricated without using the MaCE process.

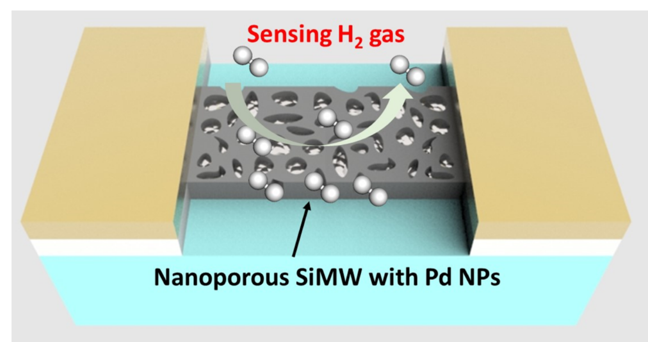

Figure 1. Schematic of proposed hydrogen (H_2) sensor based on the nanoporous SiMW decorated with Pd NPs.

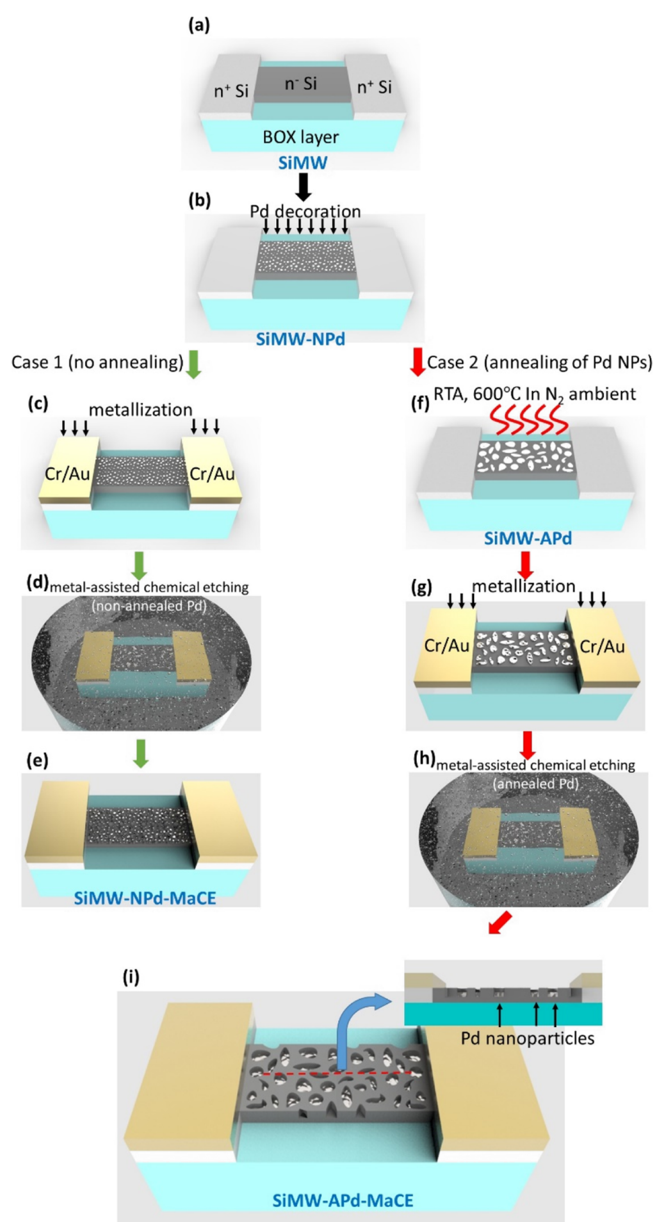

Figure 2. Schematics of the fabrication process for (a−e) SiMW-NPd-MaCE and (a,b,f−i) nanoporous SiMW-APd-MaCE: (a) SiMW defined by reactive ion etching and ion implantation processes; (b) Pd NP decoration by e-beam evaporation on SiMW; (c) Cr/Au electrode formation on SiMW-NPd; (d) MaCE of SiMW catalyzed by as-deposited Pd NPs; (e) final schematic of SiMW-NPd-MaCE; (f) Pd-decorated SiMW after the RTA process; (g) Cr/Au electrode formation on SiMW-APd; (h) selective MaCE of SiMW catalyzed by thermally annealed Pd NPs; (i) final schematic of SiMW-APd-MaCE.

2. EXPERIMENTAL WORK

2.1. Device Fabrication. *2.1.1. SiMW Decorated with Pd NPs.* A p-type silicon-on-insulator wafer with a 50 nm thick top Si layer and 375 nm thick buried oxide layer was used for device fabrication. Si microwire (SiMW) area was patterned by photolithography with a positive photoresist (AZ 5214, MicroChemicals GmbH, Germany) followed by reactive-ion etching of the top Si layer using a mixture of O_2 and SF_6 gases (Figure 2a). The electrode regions were highly doped with arsenic (As) using an ion implantation process (energy = 25 keV, dose = 5×10^{15} cm^{-2}). SiMW channel areas were doped with phosphorus (P) by ion implantation (energy = 15 keV, dose = 5×10^{15} cm^{-2}) to achieve relatively low doping than the electrode regions. Dopant activation was performed using a RTA process (1000 °C for 10 s in N_2 ambient). A thin layer of Pd (1 nm) was deposited by electron beam (e-beam) evaporation in a vacuum (pressure ~ 10^{-6} Torr) on the SiMW channel area (Figure 2b), which resulted in the formation of Pd NP clusters.

2.1.2. SiMW Decorated with Nonannealed Pd after MaCE (SiMW-NPd-MaCE). Metal contacts are formed by depositing 20 nm of chromium (Cr) and 200 nm of gold (Au) layers with e-beam evaporation on the source and drain areas (Figure 2c). MaCE method was used to chemically etch the SiMW channel area using as-deposited and nonannealed Pd NPs as a catalyst (Figure 2d). The SiMW channel with annealed Pd NPs was immersed in the etchant for 25 s. To prepare the etchant, deionized water, HF (49% by weight, J. T. Baker, United States), and H_2O_2 (30% by weight, J. T. Baker, United States) were mixed with a ratio of 5000:500:1 by volume in a clean room with controlled temperature and humidity (21 °C, 40% humidity). The etching time was optimized so that the top Si layer is not fully etched, but a roughened Si surface with a sufficient surface area is generated for chemical reaction with the target gas.

2.1.3. SiMW Decorated with Annealed Pd after MaCE (SiMW-APd-MaCE). After Pd decoration on the SiMW (Figure 2b), annealing of the Pd-decorated SiMW was carried out using the RTA process (600 °C for 5 min in N_2 ambient) to induce the solid-state dewetting of Pd NPs (Figure 2f). Details of the temperature profile are described

https://dx.doi.org/10.1021/acsami.0c10785
ACS Appl. Mater. Interfaces 2020, 12, 43614−43623

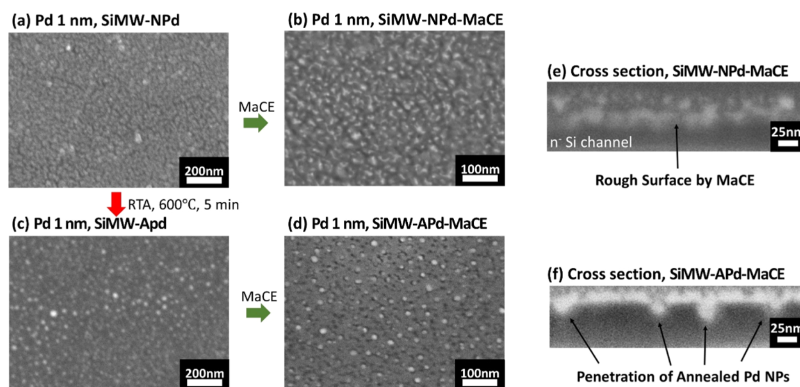

Figure 3. SEM images of (a) as-deposited Pd NPs on Si by e-beam evaporation (thickness of 1 nm); (b) chemically etched Si surface with nonannealed Pd NPs after immersing in the etching solution for 25 s; (c) Pd NPs on Si after RTA for 5 min in N_2 ambient at 600 °C; (d) chemically etched Si surface with annealed Pd NPs (thickness of 1 nm) after immersing in the etching solution for 30 s; (e) cross-section of the chemically etched Si surface with nonannealed Pd NPs; (f) cross-section of the chemically etched Si surface with annealed Pd NPs.

in the Supporting Information (Figure S1). Metal contact is formed as stated in Section 2.1.2 (Figure 2g). MaCE method was used to chemically etch the SiMW channel area using annealed Pd NPs as a catalyst (Figure 2h). The SiMW channel with annealed Pd NPs was immersed in the same etchant from Section 2.1.2 for the same etching time. The etched part of the SiMW with MaCE was coated with 50 nm of polymethylglutarimide by spin coating as a H_2-permeable protective layer.

2.2. Characterization. The *I*−*V* characteristics of fabricated devices were measured using an Agilent 4155 semiconductor analyzer (Keysight, United States). Field emission scanning electron microscopy (SU5000, Hitachi, Japan) was used to characterize the surface morphology of the sensors. Focused ion beam (FIB, Helios Nanolab, FEI, United States) was used to characterize the cross-section of the channel area of the Pd NP-decorated SiMW. Magnetic sector secondary ion mass spectrometry (SIMS, IMS 7f, CAMECA, France) was utilized to examine the Pd impurity in the Si thin film.

2.3. Gas Sensing Experiment. Gas detection experiment was carried out in a sealed chamber with a gas outlet and inlet. The flow rate was controlled by mass flow controllers (MFCs). The volume ratio of N_2 and O_2 was maintained as 4:1 to mimic the ambient air environment, while the total flow rate was fixed at 500 sccm. The voltage was applied via a sourcemeter (2635B, Keithley, United States) to collect real-time current response. Both MFCs and the sourcemeter were controlled by LabView (National Instruments, United States) interface. Detailed schematic is described in the Supporting Information (Figure S2).

3. RESULTS AND DISCUSSION

Si surfaces with Pd NPs and nanoporous Si surfaces after MaCE were observed with scanning electron microscopy (SEM) (Figure 3). By depositing Pd with e-beam evaporation (thickness = 1 nm), densely packed Pd NPs were formed on the surface of the SiMW (SiMW decorated with nonannealed Pd NPs: SiMW-NPd) (Figure 3a). RTA process was performed on the SiMW with Pd NPs, resulting in loosely located NPs with larger sizes on the surface of the SiMW (SiMW decorated with annealed Pd NPs: SiMW-APd) (Figure 3c). This agrees with atomic force microscopy images that confirm the diffusion and nucleation of densely located Pd NPs into larger NPs with low density by thermal annealing process as reported by Kunwar, et al.[25] For annealed Pd NPs, we analyzed the distribution of particle diameters with an image processing program (Figure S4). To check the diffusion of Pd impurity into the SiMW during the RTA process, SIMS analysis was carried out for SiMW-NPd and SiMW-APd (Figure S5). The intensity of Pd inside the SiMW did not change before and after the RTA process. It can be assumed that the diffusion of Pd into the Si layer during the annealing process is negligible.

Subsequently, the SiMW with Pd NPs was immersed in the etching solution to generate a nanoporous Si film (Figure 3b,d). Both Pd-SiMWs with and without thermal annealing were treated with MaCE. In Pd-based MaCE, decorated Pd NPs act like catalysts to oxidize the Si surface so that HF in the etchant can remove the oxidized Si around the Pd NPs. The chemical reaction during MaCE can be described as following[11,23]

At Pd (cathode)

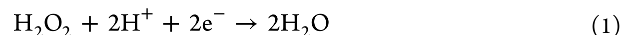

$$H_2O_2 + 2H^+ + 2e^- \rightarrow 2H_2O \quad (1)$$

At Si (anode)

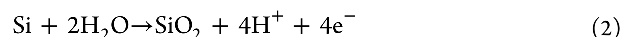

$$Si + 2H_2O \rightarrow SiO_2 + 4H^+ + 4e^- \quad (2)$$

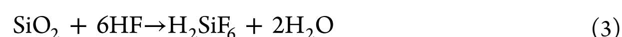

$$SiO_2 + 6HF \rightarrow H_2SiF_6 + 2H_2O \quad (3)$$

SiMW decorated with nonannealed Pd after MaCE (SiMW-NPd-MaCE) showed a surface with nanoscale roughness (Figure 3b). To investigate the exact feature, a cross-section of the etched surface was prepared by FIB (Figure 3e). The etched surface of SiMW-NPd-MaCE exhibited a small surface roughness. In comparison, SiMW decorated with annealed Pd after MaCE (SiMW-APd-MaCE) had higher surface roughness with distinct nanosized holes (Figure 3f). From the cross-sectional view, it is clearly seen that holes were created in the vicinity of the aggregated Pd NPs. Here, Pd NPs were used as a catalyst in the MaCE process. Moreover, these NPs remained in the etched holes on the surface so that they could act as a chemical gate for the H_2 gas detection.

The difference between the surfaces of SiMW-NPd-MaCE and SiMW-APd-MaCE can be explained as follows. After the annealing of Pd NPs, (i) dewetting of Pd NPs arranges the distances between nanoparticles and (ii) adhesion between Si and Pd NPs is improved. The as-deposited Pd NPs are densely packed so that during the etching, the whole surface would be etched to create nanoscale roughness. Also, the as-deposited NPs would be relatively smaller and have lower adhesion. Thus, NPs can freely move along the surface during the MaCE, affecting the whole surface. Meanwhile, aggregation of Pd NPs because of dewetting would etch the Si near the gathered Pd NPs. In addition, because of better adhesion by thermal

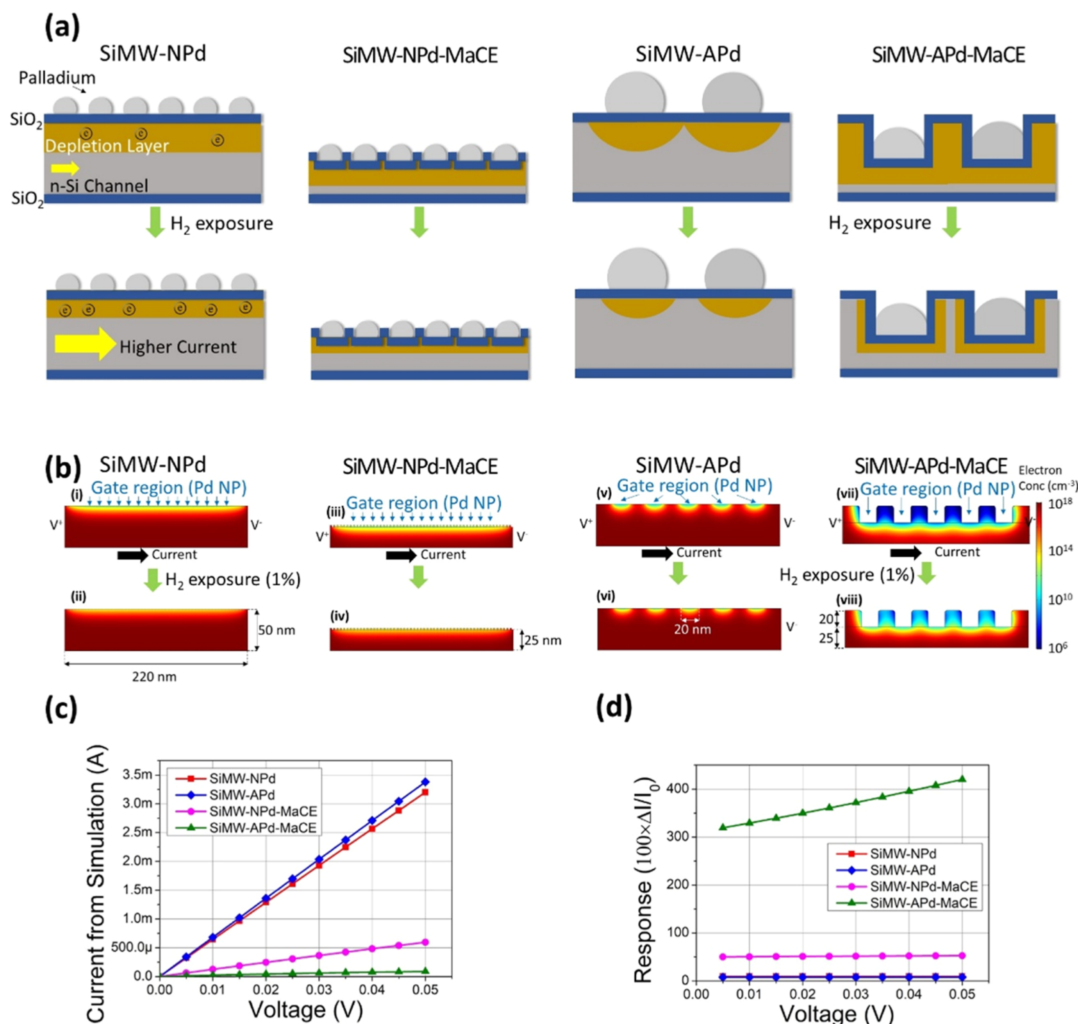

Figure 4. Schematic models and simulation results of Pd-decorated SiMW devices in different fabrication steps: (a) schematics of the effect of annealed or as-deposited Pd NPs on the depletion layer of SiMW before and after MaCE; (b) numerical simulation of the electron concentration of annealed or as-deposited Pd-decorated SiMWs before and after MaCE upon air or H_2 exposure. For the Pd NP gate, it is assumed that in air, the work function of Pd, ϕ_{Pd}, is 5.2 eV, and in 1% of H_2 atmosphere, ϕ_{Pd} is 5.04 eV, with no external gate voltage applied; (c) comparison of the simulation results for the voltage bias across the electrodes vs electrical current of SiMW-NPd, SiMW-NPd-MaCE, SiMW-APd, and SiMW-APd-MaCE in ambient air (ϕ_{Pd} = 5.2 eV); (d) summary of the simulation results for voltage bias across the electrodes vs response upon exposure to 1% H_2 of SiMW-NPd, SiMW-NPd-MaCE, SiMW-APd, and SiMW-APd-MaCE.

annealing, the Pd NPs would remain in their position during the MaCE process. As observed in Figure 3e, the aggregated NPs remained in the etched holes.

To interpret the influences of Pd annealing, MaCE of SiMW, and their combinations, numerical simulations (COMSOL Multiphysics) were performed for the calculation of the electron concentration and electrical current of SiMW-NPd, SiMW-NPd-MaCE, SiMW-APd, and SiMW-APd-MaCE (Figure 4). Pd NPs decorated on the Si surface form a depletion layer in the SiMW because of its high work function. These Pd NPs can act as a chemical gate by the difference of work functions between ambient air and H_2 environments. This chemical gating effect is represented as the reduction of the depletion layer (Figure 4a). A rectangular Si channel with 220 nm length and 50 nm height represented a small portion of the SiMW, which is 1/100 of the original channel length. The Pd NPs were considered as electrical gates with a very thin insulator (1 nm thin SiO_2 film). The sizes of Pd NPs are set as 2 nm and 20 nm for nonannealed Pd NPs and annealed Pd NPs, respectively. A voltage bias of 0−0.05 V was applied between the left and right sides of the SiMW. The work function of Pd was set as 5.2 eV in the ambient air and 5.04 eV in 1% H_2.[26] As shown in the simulation result, the region near the Pd gates was depleted. For SiMW-NPd, SiMW-NPd, and SiMW-APd, the Pd chemical gates only affected the Si beneath the Pd NPs (Figure 4bi,iii,v). Meanwhile, for SiMW-APd-MaCE, Pd NPs in the nanopores created a wider depletion region because of contact with the sidewalls of nanopores on the SiMW. The vertical edge of Si near the Pd NPs was greatly affected leading to the formation of a depletion region (Figure 4bviii). We compared the total electrical current versus voltage bias of four different cases calculated from the simulation (Figure 4c). By comparison, it can be qualitatively inferred that the electrical resistance increases after MaCE. For all devices, the depletion region was reduced (Figure 4bii,iv,vi,viii) by the exposure to H_2 gas because of the lower work function of palladium hydride (PdH_x) as compared to that of pure Pd. However, the effect is much greater for SiMW-APd-MaCE (Figure 4bviii). The relative change of total current before and after 1% H_2 exposure is summarized for four different cases

https://dx.doi.org/10.1021/acsami.0c10785
ACS Appl. Mater. Interfaces 2020, 12, 43614−43623

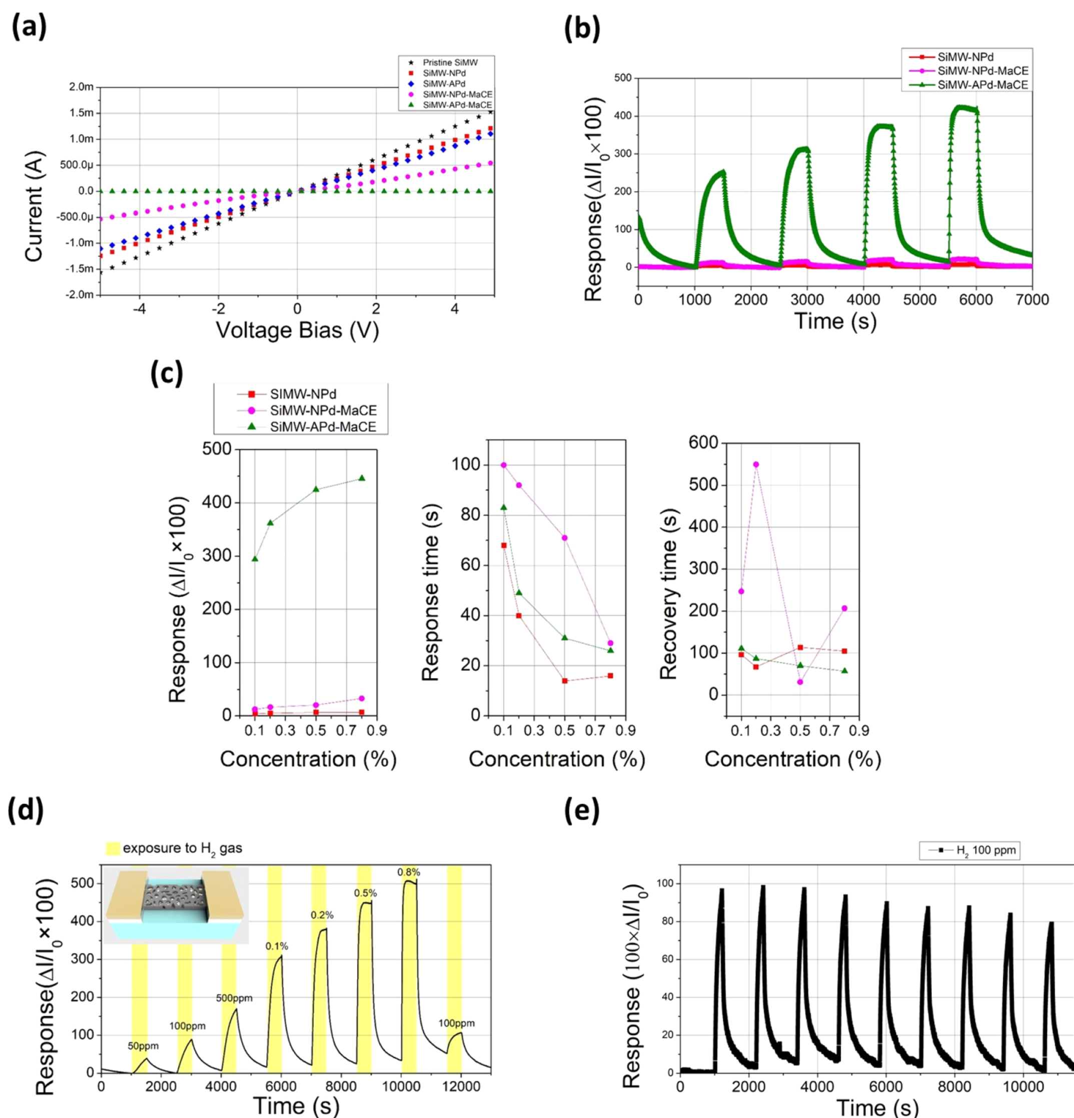

Figure 5. Electrical characterization and sensing responses of fabricated sensors upon H_2 exposure: (a) $I-V$ curves of SiMW devices with different fabrication steps (pristine SiMW, SiMW-NPd, SiMW-APd, SiMW-NPd-MaCE, and SiMW-APd-MaCE); (b) dynamic real-time response of sensors (SiMW-NPd, SiMW-NPd-MaCE, and SiMW-APd-MaCE) to H_2 gas with concentrations of 0.1, 0.2, 0.5, and 0.8%; (c) response and response time of SiMW-NPd, SiMW-NPd-MaCE, and SiMW-APd-MaCE sensors; (d) dynamic response of SiMW-APd-MaCE to H_2 with concentrations of 50 ppm to 0.8%; (e) repeatability test of SiMW-APd-MaCE for 100 ppm of H_2.

(Figure 4d). Here, the relative change of the current is represented as the response, which is defined as

$$\text{response} = \frac{I_{sat} - I_{air}}{I_{air}} \times 100 = \frac{\Delta I}{I_0} \times 100 \quad (4)$$

where I_{air} represents the electrical current in the ambient air and I_{sat} represents the saturation current in the H_2 environment. SiMW-APd-MaCE was expected to have a superior response ($\Delta I/I_0$ = 420% at a bias of 0.05 V) upon exposure to H_2 environment than SiMW-NPd ($\Delta I/I_0$ = 9.38% at a bias of 0.05 V), SiMW-APd ($\Delta I/I_0$ = 7.77% at a bias of 0.05 V), and SiMW-NPd-MaCE ($\Delta I/I_0$ = 52.7% at a bias of 0.05 V).

We measured the electrical characteristics of SiMW devices for each fabrication step—pristine SiMW, SiMW-NPd, SiMW-APd, SiMW-NPd-MaCE, and SiMW-APd-MaCE (Figure 5a). The width, length, and thickness of the SiMW were 20 μm, 20 μm, and 50 nm, respectively (Figure S3). Because Pd has a high work function (ϕ_{Pd} ~ 5.2 eV), Schottky barrier forms between Pd and Si, and the depletion layer arises from the metal−semiconductor junction at the interfacial layer of Si.[27] This depletion hinders the electrical current through the SiMW, thus resulting in higher electrical resistance of Pd-decorated SiMWs. The RTA process did not greatly influence the electrical resistance of the SiMW. After the MaCE process, the resistance was greatly increased. For SiMW-NPd-MaCE, this increase in electrical resistance is because of the reduction of the layer thickness and nanoscale roughness. However, for SiMW-APd-MaCE, the major resistance change is attributed to the penetration of Pd NPs in the middle of SiMW so that the remaining sidewalls are greatly affected by these Pd NPs. We expected that if these Pd NPs can penetrate the Si thin film, then a higher portion of the Si film would be affected by Pd NPs to generate a greater depleted region. In addition, the depleted region would be affected by the change in the work function of Pd, which varies upon exposure to H_2.

To investigate the sensing characteristics of proposed devices for H_2 gas, gas-sensing tests were conducted with

https://dx.doi.org/10.1021/acsami.0c10785
ACS Appl. Mater. Interfaces 2020, 12, 43614−43623

various concentrations of H_2 gas mixed with synthetic air. In this test, we compared the sensing performances of SiMW-NPd, SiMW-NPd-MaCE, and SiMW-APd-MaCE (Figure 5b,c). It is certain that, after the MaCE process, the sensor response is improved for both of SiMW-NPd-MaCE and SiMW-APd-MaCE. In addition, the SiMW-APd-MaCE device showed a much higher response than SiMW-NPd-MaCE. During the exposure to H_2 with a concentration of 0.8%, SiMW-APd-MaCE achieved a superior response of 446%, which is 62.8 times larger than that of SiMW-NPd. It should be noted that an operating voltage of 5 V was used for SiMW-APd-MaCE. It showed a very low power consumption (1.62 μW) during the idle state, and the maximum power consumption was as low as 5.35 μW for 0.8% H_2, which is a great advantage for the sensor operation. The repeatability test was carried out for SiMW-APd-MaCE with 100 ppm of H_2 (Figure 5e), which showed consistent responses with repeated exposure to H_2.

When comparing the response data of the gas-sensing test with the simulation results that are explained above, they show a good agreement with each other (Figure 6). Despite the difference of H_2 concentration between the simulation and gas test, it shows a similar trend that the combination of Pd annealing and MaCE allows for superior response compared to the nonannealed case.

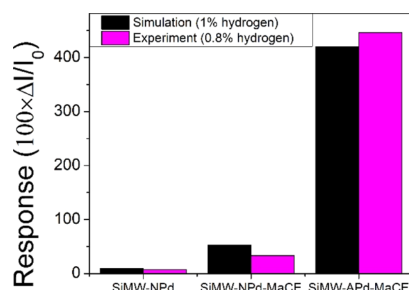

Figure 6. Comparison of response between the 2D numerical simulation (1% H_2) and the experimental result (0.8% H_2).

The increased response of SiMW-NPd-MaCE can be explained by the (i) increased surface-to-volume ratio and (ii) reduction in the thickness of the Si layer. From the top view and cross-sectional view of SiMW-NPd-MaCE (Figure 3), the surface of SiMW-NPd-MaCE has a high surface-to-volume ratio with nanoscale roughness. Additionally, the total thickness of the SiMW decreases as a result of etching catalyzed by closely located Pd NPs. The depletion layer thickness would be the same, although the total Si thickness is trimmed. Thus, the ratio of Si affected by Pd increases so that it would have a higher response during the exposure to H_2.[28]

Meanwhile, the improved response of SiMW-APd-MaCE would be mostly attributed to the penetration of Pd NPs into the middle of the Si layer while increasing its surface roughness. From the calculation, the depletion layer thickness of Si contacted with Pd is around 10 nm. If the Pd NPs are on the surface, they only affect the Si beneath the particles. However, if the Pd NPs penetrate the middle of the Si layer, then the depleted volume of Si affected by Pd would be larger, as it is predicted from the numerical simulation of electron concentration in Figure 4.

The response and recovery times were calculated as the elapsed time from 20 to 80% of the difference between H_2 saturation and ambient air states. SiMWs treated with MaCE (SiMW-NPd-MaCE and SiMW-APd-MaCE) showed slower response and recovery time than the flat SiMW-NPd. For the SiMW-NPd, 20 to 80% response time was 16 s for 0.8% of H_2. For SiMW-NPd-MaCE and SiMW-APd-MaCE, the response time was 29 and 26 s, respectively (Figure 5c). This slowdown in response and recovery time is common in many SiNW gas sensors fabricated by MaCE.[24,29,30] The surface of SiMW with MaCE has nanopores, in which the H_2 adsorption of Pd NPs is hindered. From the SEM images in Figure 3d,e, the diameter of the pore lay in the range of 8 to 26 nm. In this range of pore size, Knudsen diffusion is the dominant regime since the mean free path in the atmosphere is larger than the pore size.[31,32] A highly nanoporous surface of etched SiMW deters the diffusion of H_2 molecules so that it takes much more time for Pd NPs to reach the saturation point for H_2 absorption.[33−35] Therefore, we expect that the response and recovery time could be enhanced by creating a larger pore with larger Pd NPs to reduce the effect of the Knudsen diffusion regime.

To demonstrate that the SiMW-APd-MaCE sensor is selective for H_2 against other gases, with NH_3, HF, NO_2, HCl, and CO, we performed gas tests with those gases (Figure

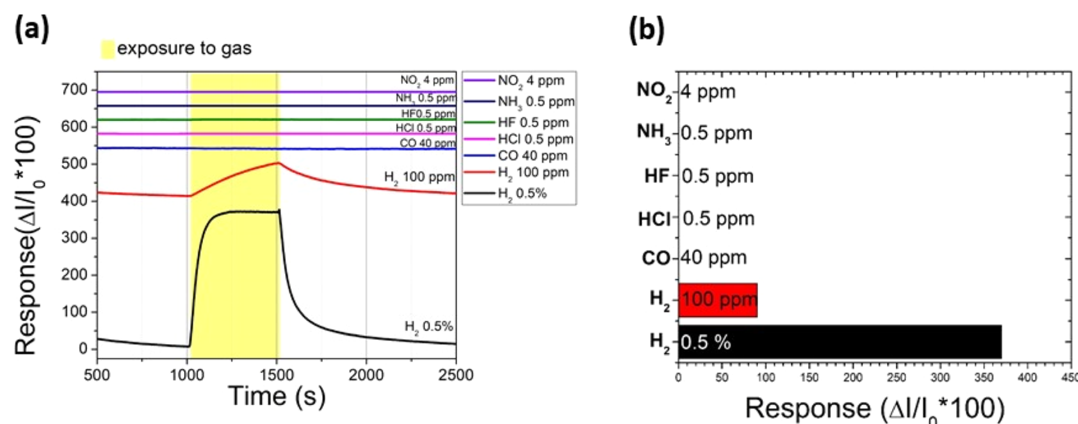

Figure 7. Selectivity characterization of SiMW-APd-MaCE sensor: (a) real-time responses of SiMW-APd-MaCE sensor to different gases (H_2, NH_3, HF, NO_2, HCl, and CO); (b) selective responses of the sensor against other interfering gases. The sensor showed $\Delta I/I_0$ of 370 and 90% to H_2 gas with concentrations of 0.5% and 100 ppm, respectively. In comparison, it showed no response to NH_3 (0.5 ppm), HF (0.5 ppm), NO_2 (4 ppm), HCl (0.5 ppm), and CO (40 ppm). Here, these gas concentrations were selected by the TWA exposure limit according to NIOSH.

https://dx.doi.org/10.1021/acsami.0c10785
ACS Appl. Mater. Interfaces 2020, 12, 43614−43623

Table 1. Comparison of Recently Reported H_2 Gas Sensors Based on Pd-Decorated Si, Carbon Nanotubes, Metal Oxides, and Graphene

materials	fabrication method	response ($[H_2] \sim 0.1\%$)	response ($[H_2] \sim 1\%$)	dynamic range[a]	t_{res}/t_{rec} ($[H_2] \sim 1\%$)	selectivity[b]	operating temperature	power consumption	refs
Pd NP @ rough Si	Pd annealing &MaCE	294%	446%	50 ppm-0.8%	32 s/110 s	NO_2, NH_3, HF, HCl, CO	RT	1.62 μW	this work
Pd NP @ vertically aligned-SiNWs	Ag-MaCE & Pd coating	320%	1700%	5 ppm-1%	N/A	N/A	RT	N/A	24
Pd NP @ Si nanomesh	nanosphere lithography	10%	27%	50 ppm-0.8%	5 s/13 s	H_2S, NO_2, CO, toluene, ethanol	RT	400 μW	15
Pd NP @ SiNW	e-beam lithography	0.8%	N/A	0.1−1%	5 s/13 s	N/A	RT	1.04 μW	37
Pd&; Au NP @ Si thin film	oxidation & etching	90%	550%	0.3−2%	40 s/×	NO_2	RT	0.34 nW	28
Pd-MWCNTcomposite	chemical vapor deposition (CVD)	0.22%	0.35%	0.1−10%	85 s/×	N/A	RT	N/A	38
Pd @ WO_3 nanofiber	electrospinning	N/A	N/A	10−500 ppm	N/A	CH_4, CO, NH_3	450 °C	N/A (furnace is used)	39
ZnO−SnO_2 composite	electrospinning and annealing	50%	90%	0.1−1%	65 s/80 s	not selective	150 °C	N/A (external heater)	40
Pd @ graphene	CVD	N/A	5.88%	1−4%	180 s/540 s	CH_2ONH_3	RT	0.98 mW (external light)	41
Pd nanofiber	electrospinning & e-beam evaporation	N/A	0.95%	0.8−1.8%	28 s/×	NH_3, CO, NO_2, H_2S	RT	N/A	42

[a]Here, the dynamic range described in this table is based on the experimental range used in each paper. This does not exactly represent the lower and upper detection limits. [b]The gases listed in the column "selectivity" are those the sensor does not show any response to.

https://dx.doi.org/10.1021/acsami.0c10785
ACS Appl. Mater. Interfaces 2020, 12, 43614−43623

7). The concentration of each gas was selected based on the time-weighted average (TWA) exposure limit according to the National Institute for Occupational Safety and Health of the United States (NIOSH).[36] It was verified that the SiMW-APd-MaCE sensor shows almost no response to other gases except H_2. This confirms that the suggested sensor can selectively detect H_2 gas from other interfering species because of the natural inertness of Si to these gases and the selective absorption property of Pd with H_2.

We compared recently reported H_2 sensors based on the pure Pd nanostructures or Pd-decorated Si, carbon nanotubes, metal oxides, and graphene in Table 1. Si/Pd-NP-based sensors have several advantages among several potential H_2-sensing materials. First, they show relatively faster responses and recoveries. When using decoration of Pd NPs, absorption of H_2 only occurs on the surface of the sensors, considering that Si is inert to H_2, which can contribute to the fast response and recovery. Moreover, the inertness of Si to most of the gases allows us a good selectivity to a particular target gas. Pure Pd nanostructures are common sensing materials for the selective and room-temperature hydrogen sensing. However, since the sensing mechanism relies on the hydrogenation of Pd, achieving a low detection limit is difficult and the response is usually low. Metal oxides are widely used for many gas-sensing applications because of their high response to various gases. Yet, they suffer from poor selectivity and high operation temperature that leads to high operating power for external heaters. Compared to the previously developed Pd-based H_2 sensors, our sensor exhibited a high response and a large dynamic range. Furthermore, we realized a facile fabrication of high-performance H_2 sensors with annealing of Pd NPs and short-time MaCE of the Si thin film, which could greatly reduce the fabrication cost compared to the high-resolution nanopatterning or chemical synthesis of nanostructures. In addition, our room-temperature-operating sensor showed a high response with a very low operating power. Although slow response and recovery speeds limit the MaCE-based sensors, a simple fabrication process and scalability to inexpensive large volume manufacturing processes are major advantages of this approach.

4. CONCLUSIONS

In conclusion, a H_2 sensor with high performance, low power, and room-temperature sensing capability was developed through a low-cost and simple fabrication method based on Pd-assisted chemical etching. The nanoporous surface of the Si thin film and penetration of Pd NPs into the Si film increased the chemical gating effect of Pd. Annealing of Pd NPs by RTA process induced the dewetting process of the densely packed Pd NPs leading to larger particles, resulting in longer distances between them. After MaCE with annealed Pd NPs, a nanoporous Si film was achieved, rather than a rough surface by nonannealed-Pd MaCE. Combining the annealed Pd NPs with MaCE enabled the dramatic improvement of sensor response for 0.1% of H_2 by 62.8 times that of the original flat Si film decorated with Pd NPs and 23 times that of the nonannealed-Pd MaCE. This SiMW-APd-MaCE sensor operates with a very low power of 1.62 μW, which is a great advantage for potential mobile applications. In addition, the nanoporous Si thin film device did not use any expensive lithography method for high-resolution patterning because of the facile Pd-based MaCE process. Because Pd is selective to H_2, the SiMW decorated with annealed Pd after MaCE showed good selectivity to H_2 gas against other gases. The SiMW-APd-MaCE sensors can be fabricated at relatively low cost compared to other existing methods. We expect that our approach would be applicable to large-scale fabrication of H_2 sensors based on Si film because of its CMOS compatibility. This method would also be useful for other future applications for high-performance and low-cost chemical and biological sensors.

■ ASSOCIATED CONTENT

Supporting Information

The Supporting Information is available free of charge at https://pubs.acs.org/doi/10.1021/acsami.0c10785.

Intended temperature profile for RTA process, schematic diagram of the gas experiment setup, photos of fabricated SiMW device, Pd NPs on Si after rapid thermal annealing for 5 min in N_2 ambient at 600 °C, particle analysis using ImageJ program, particle size distribution of annealed Pd NPs, SIMS profile of Si with Pd NPs deposited by e-beam evaporation, and schematics of sensing mechanism describing the changes in the electrical conductance of Pd decorated silicon channel with or without H_2 gas exposure (PDF)

■ AUTHOR INFORMATION

Corresponding Author

Inkyu Park − *Department of Mechanical Engineering, Korea Advanced Institute of Science and Technology, Daejeon 34141, Republic of Korea;* orcid.org/0000-0001-5761-7739; Phone: +82-42-350-3240; Email: inkyu@kaist.ac.kr

Authors

Hyeonggyun Kim − *Department of Mechanical Engineering, Korea Advanced Institute of Science and Technology, Daejeon 34141, Republic of Korea*

Jeonghoon Yun − *School of Chemical and Biomedical Engineering and Singapore Membrane Technology Center, Nanyang Technological University, 639798, Singapore*

Min Gao − *Department of Mechanical Engineering, Korea Advanced Institute of Science and Technology, Daejeon 34141, Republic of Korea*

Hyeok Kim − *School of Electrical and Computer Engineering, University of Seoul, Seoul 02592, Republic of Korea*

Minkyu Cho − *Department of Mechanical Engineering, Korea Advanced Institute of Science and Technology, Daejeon 34141, Republic of Korea;* orcid.org/0000-0002-0006-2063

Complete contact information is available at: https://pubs.acs.org/10.1021/acsami.0c10785

Author Contributions

The manuscript was written through the contributions of all authors. All authors have given approval to the final version of the manuscript.

Notes

The authors declare no competing financial interest.

■ ACKNOWLEDGMENTS

This research was supported by Nano Material Technology Development Program (2015M3A7B7045518) through the National Research Foundation of Korea (NRF) funded by the Ministry of Science, ICT & Future Planning, Multi-Ministry Collaborative R&D Program (Development of Techniques for

Identification and Analysis of Gas Molecules to Protect Against Toxic Substances) through the NRF funded by KNPA, MSIT, MOTIE, ME, NFA (NRF-2017M3D9A1073858), and Development of Management Technology for HNS Accident (D11502815H480000140 2015034016) funded by the Ministry of Oceans and Fisheries, Korea.

■ REFERENCES

(1) Li, Y.; Qian, F.; Xiang, J.; Lieber, C. M. Nanowire Electronic and Optoelectronic Devices. *Mater. Today* **2006**, *9*, 18−27.

(2) Chen, R.; Li, D.; Hu, H.; Zhao, Y.; Wang, Y.; Wong, N.; Wang, S.; Zhang, Y.; Hu, J.; Shen, Z.; Xiong, Q. Tailoring Optical Properties of Silicon Nanowires by Au Nanostructure Decorations: Enhanced Raman Scattering and Photodetection. *J. Phys. Chem. C* **2012**, *116*, 4416−4422.

(3) Peng, K.; Xu, Y.; Wu, Y.; Yan, Y.; Lee, S.-T.; Zhu, J. Aligned Single-Crystalline Si Nanowire Arrays for Photovoltaic Applications. *Small* **2005**, *1*, 1062−1067.

(4) Chan, C. K.; Peng, H.; Liu, G.; McIlwrath, K.; Zhang, X. F.; Huggins, R. A.; Cui, Y. High-Performance Lithium Battery Anodes Using Silicon Nanowires. *Nat. Nanotechnol.* **2008**, *3*, 31−35.

(5) Park, I.; Li, Z.; Li, X.; Pisano, A. P.; Williams, R. S. Towards the Silicon Nanowire-Based Sensor for Intracellular Biochemical Detection. *Biosens. Bioelectron.* **2007**, *22*, 2065−2070.

(6) Park, I.; Li, Z.; Pisano, A. P.; Williams, R. S. Top-down Fabricated Silicon Nanowire Sensors for Real-Time Chemical Detection. *Nanotechnology* **2010**, *21*, 015501.

(7) Cui, Y.; Wei, Q.; Park, H.; Lieber, C. M. Nanowire Nanosensors for Highly Sensitive and Selective Detection of Biological and Chemical Species. *Science* **2001**, *293*, 1289−1292.

(8) Stern, E.; Klemic, J. F.; Routenberg, D. A.; Wyrembak, P. N.; Turner-Evans, D. B.; Hamilton, A. D.; LaVan, D. A.; Fahmy, T. M.; Reed, M. A. Label-Free Immunodetection with CMOS-Compatible Semiconducting Nanowires. *Nature* **2007**, *445*, 519−522.

(9) Cui, Y.; Zhong, Z.; Wang, D.; Wang, W. U.; Lieber, C. M. High Performance Silicon Nanowire Field Effect Transistors. *Nano Lett.* **2003**, *3*, 149−152.

(10) Li, W.; Xu, L.; Zhao, W.-M.; Sun, P.; Huang, X.-F.; Chen, K.-J. Fabrication of Large-Scale Periodic Silicon Nanopillar Arrays for 2D Nanomold Using Modified Nanosphere Lithography. *Appl. Surf. Sci.* **2007**, *253*, 9035−9038.

(11) Chartier, C.; Bastide, S.; Lévy-Clément, C. Metal-Assisted Chemical Etching of Silicon in HF−H2O2. *Electrochim. Acta* **2008**, *53*, 5509−5516.

(12) Mikolajick, T.; Weber, W. M. *Anisotropic Nanomaterials*, Springer International Publishing: 2015.

(13) Ramgir, N. S.; Yang, Y.; Zacharias, M. Nanowire-Based Sensors. *Small* **2010**, *6*, 1705−1722.

(14) Lundström, I.; Shivaraman, S.; Svensson, C.; Lundkvist, L. A Hydrogen-Sensitive MOS Field-Effect Transistor. *Appl. Phys. Lett.* **1975**, *26*, 55−57.

(15) Gao, M.; Cho, M.; Han, H.-J.; Jung, Y. S.; Park, I. Palladium-Decorated Silicon Nanomesh Fabricated by Nanosphere Lithography for High Performance, Room Temperature Hydrogen Sensing. *Small* **2018**, *14*, 1703691.

(16) Ahn, J.-H.; Yun, J.; Choi, Y.-K.; Park, I. Palladium Nanoparticle Decorated Silicon Nanowire Field-Effect Transistor with Side-Gates for Hydrogen Gas Detection. *Appl. Phys. Lett.* **2014**, *104*, 013508.

(17) Yun, J.; Jin, C. Y.; Ahn, J. H.; Jeonb, S.; Park, I. Self-Heated Silicon Nanowire Array Selective Surface Modification with Catalytic Nanoparticles by Nanoscale Joule Heating and Its Gas Sensing Applications. *Nanoscale* **2013**, *5*, 6851−6856.

(18) Wu, Y.; Cui, Y.; Huynh, L.; Barrelet, C. J.; Bell, D. C.; Lieber, C. M. Controlled Growth and Structures of Molecular-Scale Silicon Nanowires. *Nano Lett.* **2004**, *4*, 433−436.

(19) Hobbs, R. G.; Petkov, N.; Holmes, J. D. Semiconductor Nanowire Fabrication by Bottom-up and Top-down Paradigms. *Chem. Mater.* **2012**, *24*, 1975−1991.

(20) Saccheto, D.; Ben-Jamaa, H.; De Micheli, G.; Leblebici, Y. Fabrication and Characterization of Vertically Stacked Gate-All-Around Si Nanowire FET Arrays. *2009 Proceedings of the European Solid State Device Research Conference*, 2009; pp 245−248.

(21) Kim, S. O.; Solak, H. H.; Stoykovich, M. P.; Ferrier, N. J.; De Pablo, J. J.; Nealey, P. F. Epitaxial Self-Assembly of Block Copolymers on Lithographically Defined Nanopatterned Substrates. *Nature* **2003**, *424*, 411−414.

(22) Li, X.; Bohn, P. W. Metal-Assisted Chemical Etching in HF/H2O2 Produces Porous Silicon. *Appl. Phys. Lett.* **2000**, *77*, 2572.

(23) Huang, Z.; Geyer, N.; Werner, P.; De Boor, J.; Gösele, U. Metal-Assisted Chemical Etching of Silicon: A Review. *Adv. Mater.* **2011**, *23*, 285−308.

(24) Baek, J.; Jang, B.; Kim, M. H.; Kim, W.; Kim, J.; Rim, H. J.; Shin, S.; Lee, T.; Cho, S.; Lee, W. High-Performance Hydrogen Sensing Properties and Sensing Mechanism in Pd-Coated p-Type Si Nanowire Arrays. *Sens. Actuators, B* **2018**, *256*, 465−471.

(25) Kunwar, S.; Pandey, P.; Sui, M.; Zhang, Q.; Li, M.-Y.; Lee, J. Effect of Systematic Control of Pd Thickness and Annealing Temperature on the Fabrication and Evolution of Palladium Nanostructures on Si (111) via the Solid State Dewetting. *Nanoscale Res. Lett.* **2017**, *12*, 364.

(26) Behzadi pour, G.; Fekri aval, L. Highly Sensitive Work Function Hydrogen Gas Sensor Based on PdNPs/SiO2/Si Structure at Room Temperature. *Results Phys.* **2017**, *7*, 1993−1999.

(27) Skucha, K.; Fan, Z.; Jeon, K.; Javey, A.; Boser, B. Palladium/Silicon Nanowire Schottky Barrier-Based Hydrogen Sensors. *Sens. Actuators, B* **2010**, *145*, 232−238.

(28) Fahad, H. M.; Shiraki, H.; Amani, M.; Zhang, C.; Hebbar, V. S.; Gao, W.; Ota, H.; Hettick, M.; Kiriya, D.; Chen, Y.-Z.; Chueh, Y.-L.; Javey, A. Room Temperature Multiplexed Gas Sensing Using Chemical-Sensitive 3.5-Nm-Thin Silicon Transistors. *Sci. Adv.* **2017**, *3*, No. e1602557.

(29) Qin, Y.; Wang, Y.; Liu, Y.; Zhang, X. KOH Post-Etching-Induced Rough Silicon Nanowire Array for H 2 Gas Sensing Application. *Nanotechnology* **2016**, *27*, 465502.

(30) Peng, K.-Q.; Wang, X.; Lee, S.-T. Gas Sensing Properties of Single Crystalline Porous Silicon Nanowires. *Appl. Phys. Lett.* **2009**, *95*, 243112.

(31) Jennings, S. G. The Mean Free Path in Air. *J. Aerosol Sci.* **1988**, *19*, 159−166.

(32) Knudsen, M. Die Gesetze Der Molekularströmung Und Der Inneren Reibungsströmung Der Gase Durch Röhren. *Ann. Phys.* **1909**, *333*, 75−130.

(33) Davis, D. H. Monte Carlo Calculation of Molecular Flow Rates through a Cylindrical Elbow and Pipes of Other Shapes. *J. Appl. Phys.* **1960**, *31*, 1169−1176.

(34) Malek, K.; Coppens, M.-O. Knudsen Self- and Fickian Diffusion in Rough Nanoporous Media. *J. Chem. Phys.* **2003**, *119*, 2801−2811.

(35) Gruener, S.; Huber, P. Knudsen Diffusion in Silicon Nanochannels. *Phys. Rev. Lett.* **2008**, *100*, 064502.

(36) National Institute for Occupational Safety and Health. NIOSH Recommended Exposure Limits (RELs).

(37) Ahn, J.-H.; Yun, J.; Moon, D.-I.; Choi, Y.-K.; Park, I. Self-Heated Silicon Nanowires for High Performance Hydrogen Gas Detection. *Nanotechnology* **2015**, *26*, 095501.

(38) McConnell, C.; Kanakaraj, S. N.; Dugre, J.; Malik, R.; Zhang, G.; Haase, M. R.; Hsieh, Y.-Y.; Fang, Y.; Mast, D.; Shanov, V. Hydrogen Sensors Based on Flexible Carbon Nanotube-Palladium Composite Sheets Integrated with Ripstop Fabric. *ACS Omega* **2020**, *5*, 487−497.

(39) Choi, S.-J.; Chattopadhyay, S.; Kim, J. J.; Kim, S.-J.; Tuller, H. L.; Rutledge, G. C.; Kim, I.-D. Coaxial Electrospinning of WO3 Nanotubes Functionalized with Bio-Inspired Pd Catalysts and Their Superior Hydrogen Sensing Performance. *Nanoscale* **2016**, *8*, 9159−9166.

(40) Mondal, B.; Basumatari, B.; Das, J.; Roychaudhury, C.; Saha, H.; Mukherjee, N. ZnO-SnO2 Based Composite Type Gas Sensor for Selective Hydrogen Sensing. *Sens. Actuators, B* **2014**, *194*, 389−396.
(41) Tang, X.; Haddad, P.-A.; Mager, N.; Geng, X.; Reckinger, N.; Hermans, S.; Debliquy, M.; Raskin, J.-P. Chemically Deposited Palladium Nanoparticles on Graphene for Hydrogen Sensor Applications. *Sci. Rep.* **2019**, *9*, 3653−11.
(42) Cho, M.; Zhu, J.; Kim, H.; Kang, K.; Park, I. Half-Pipe Palladium Nanotube-Based Hydrogen Sensor Using a Suspended Nanofiber Scaffold. *ACS Appl. Mater. Interfaces* **2019**, *11*, 13343−13349.

https://dx.doi.org/10.1021/acsami.0c10785
ACS Appl. Mater. Interfaces 2020, 12, 43614−43623